Electronic Supplementary Material (ESI) for Materials Horizons.

Supporting Information

Hard-to-soft transition-enhanced piezoelectricity in poly(vinylidene fluoride) via relaxor-like secondary crystals activated by high-power ultrasonication

Guanchun Rui [1], Elshad Allahyarov [2,3,4], Ruipeng Li [5], Philip L. Taylor [2,*], Lei Zhu [1,*]

[1] *Department of Macromolecular Science and Engineering, Case Western Reserve University, Cleveland, Ohio 44106-7202, United States*
[2] *Department of Physics, Case Western Reserve University, Cleveland, Ohio 44106-7909, United States*
[3] *Institut für Theoretische Physik II: Weiche Materie, Heinrich-Heine Universität Düsseldorf,*

Universitätstrasse 1, 40225 Düsseldorf, Germany

[4] *Theoretical Department, Joint Institute for High Temperatures, Russian Academy of Sciences, 13/19 Izhorskaya street, Moscow 125412, Russia*
[5] *National Synchrotron Light Source II, Brookhaven National Laboratory, Upton, New York 11973, United States*

* Corresponding authors. Emails: lxz121@case.edu (L. Zhu) and plt@case.edu (P.L. Taylor)

1. Experimental procedures

Materials and film processing. The PVDF pellets were purchased from MilliporeSigma (St. Louis, MO) and the weight-average molecular weight was 530 kDa, as reported by the vendor. The PVDF film (~40 μm thick) was fabricated by melt-compression molding at 200 °C, followed by quenching into an ice/water mixture. The quenched films were cut into rectangles (4×1 cm) for uniaxial stretching at room temperature, using an Instron Universal Testing System (Model 5965, Norwood, MA). The draw ratio and speed were 500% and 600%/min, respectively. After stretching, the thickness of the films was ~20 μm. For electrical poling, gold (Au) electrodes with a thickness of ca. 10 nm were evaporated on both sides of the film using a Quorum Q300T D Plus sputter coater (Quorum Technologies, Laughton, East Sussex, UK). Au-coated films were unidirectionally poled under 400 MV/m [i.e., 400 MV/m DC + 400MV/m (zero-to-peak) AC at 1 Hz] for at least 40 cycles to ensure a sizable $P_{r,0}$.

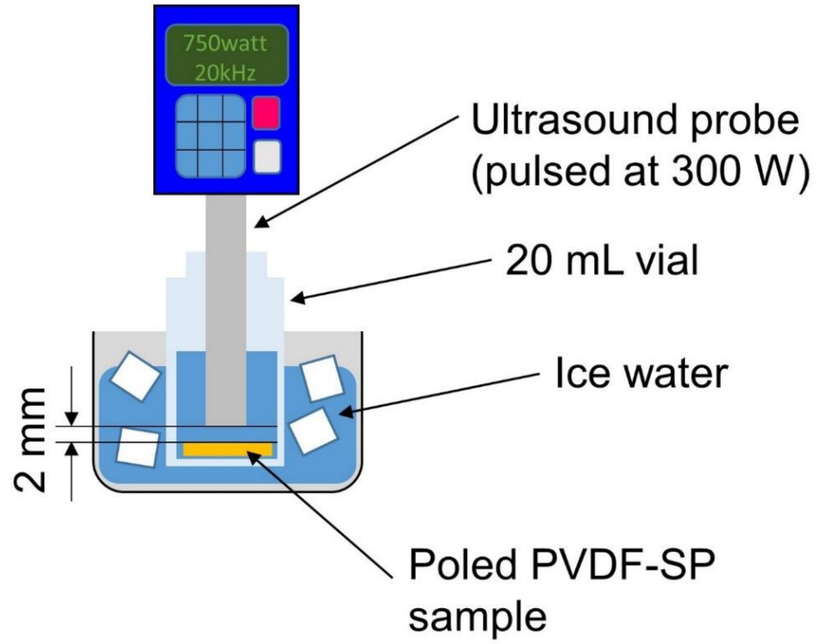

Scheme S1. Schematic representation of the ultrasonication experiment setup using a 750-W ultrasound probe at 40% power with pulses (i.e., alternating 1-s off and 5-s on). Ice was added in the water bath to prevent significant heating of the poled piezoelectric films.

The ultrasonication experiment was carried out using a Cole-Parmer 750-Watt ultrasonic processor (Antylia Scientific, Vernon Hills, IL); see Scheme S1. The poled piezoelectric film was fixed at the bottom of a 20 mL glass vial with a Kapton™ double-sided tape, and 10 mL of deionized water was then added. The ultrasound probe was inserted at a position 2 mm above the sample. The ultrasonic amplification level was set to be 40% (i.e., 300 W), and the pulse was set with 1 s of interval after 5 s of ultrasonication. To prevent overheating, an ice-water bath was used for cooling. The optimal ultrasonication power was determined by both piezoelectric performance and ultrasonic damage to the film. As shown in Fig. S1 below, the ultrasonication took effect when the power was above 100 W. The piezoelectric performance reached the maximum value of 50 pm/V around 300 W, after which the piezoelectric performance decreased. This was attributed to the ultrasonic damage of the PVDF-SPU20 film. For example, when the film was ultrasonicated at 450 W, obvious physical damage of the film was observed in the inset photo of Fig. S1b.

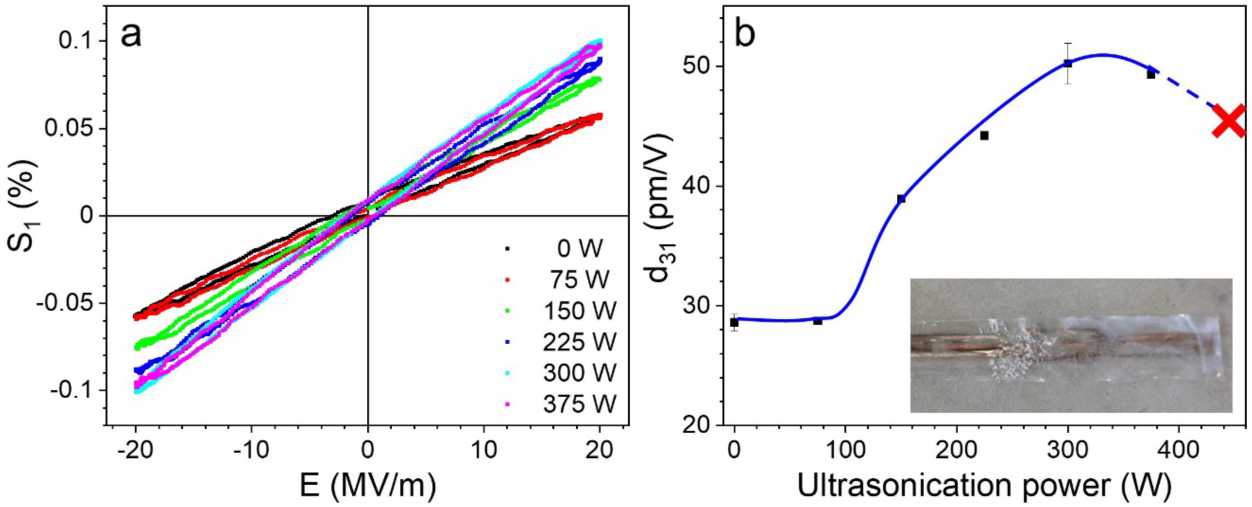

Fig. S1. Effect of ultrasonication power on the final piezoelectric performance at room temperature: (a) S_1-E loop at 1 Hz and (b) d_{31} as a function of ultrasonication power. The inset in (b) shows a photo of the PVDF-SPU20 film after ultrasonication at 450 W.

Characterization and instrumentation. Simultaneous D-E and S_1-E loop measurements were made using a Premiere II FE tester (Radiant Technologies, Inc., Albuquerque, NM) with a Trek 10/10B-HS high-voltage amplifier (0-10 kV AC, Lockport, NY), as described in previous reports.[1,2] The output voltage had a sinusoidal waveform at 1 Hz. An Au coating was applied on both sides of the film (2 mm × 15 mm) with an overlapping area of 12.0 mm^2 (2 mm × 6 mm). The Au-coated sample was installed in a home-built fixture and immersed in silicone oil to avoid corona discharge in air. The stray capacitance was determined using a biaxially oriented polypropylene film (8 μm, provided by SE Electronics, Inc., Barre, VT) and then subtracted. The S_1 was detected using a photonic sensor, MTI 2100 (MTI Instruments, Inc., Albany, NY). The temperature was controlled using a ChemGlass CG-1999-V-10 hot plate (Vineland, NJ).

DSC experiments were carried out on a Discovery DSC250 (TA Instruments, New Castle, DE). Approximately, 2 mg samples were used at a scanning rate of 10 °C/min under a dry nitrogen atmosphere (flow rate of 50 mL/min). Single-bounce diamond attenuated total reflection Fourier transform infrared (FTIR) spectra were recorded using an Agilent Cary 630 FTIR spectrometer (Agilent Technologies, Santa Clara, CA). The data were collected with 256 scans and the resolution was 4 cm^{-1}. BDS measurements were carried out on a Novocontrol Concept 80 broadband dielectric spectrometer (Montabaur, Germany) with temperature control. The output voltage was 1.0 V_{rms} (i.e., root-mean-square voltage) with frequency ranging from 1 Hz to 1 MHz and temperature from -50 to 100 °C. The samples were coated with 7.06 mm^2 of Au to minimize contact resistance. 2D SAXS and WAXD experiments were performed at the 11-BM Complex Material Scattering Beamline of the National Synchrotron Light Source II (NSLS-II), Brookhaven National Laboratory (BNL). The beam energy of the incident X-ray was 17 keV. The distances between the sample and the WAXD (Pilatus 800 K, Dectris, Gaden-Dattwil, Switzerland) and the SAXS detectors (Pilatus 2M) were 259 and 5050 mm, respectively. These distances were calibrated using silver behenate with the first-order reflection at a scattering vector of $q = (4\pi\sin\theta)/\lambda = 1.076$ nm^{-1} (θ is the half scattering angle). The typical data acquisition time was 30 s. The Y_1 was determined from stress-strain tests using the Instron Universal Testing System with a temperature control chamber.

2. Comparison of $|d_{31}|$ for different piezoelectric materials

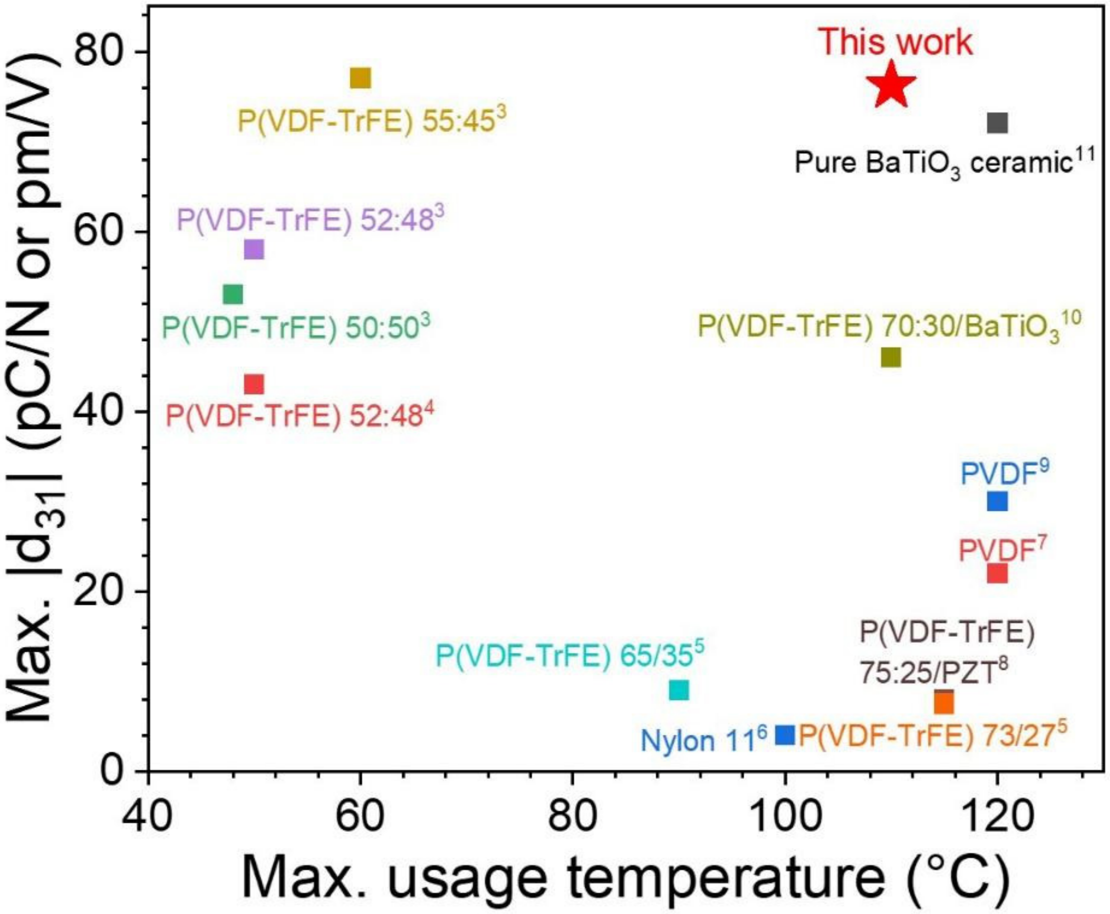

Fig. S2. Comparison of maximum $|d_{31}|$ and usage temperatures for different piezoelectric polymers and composites. The superscripts show the references (refs. 3-11).

3. Structural characterization results for the PVDF-SPUx films

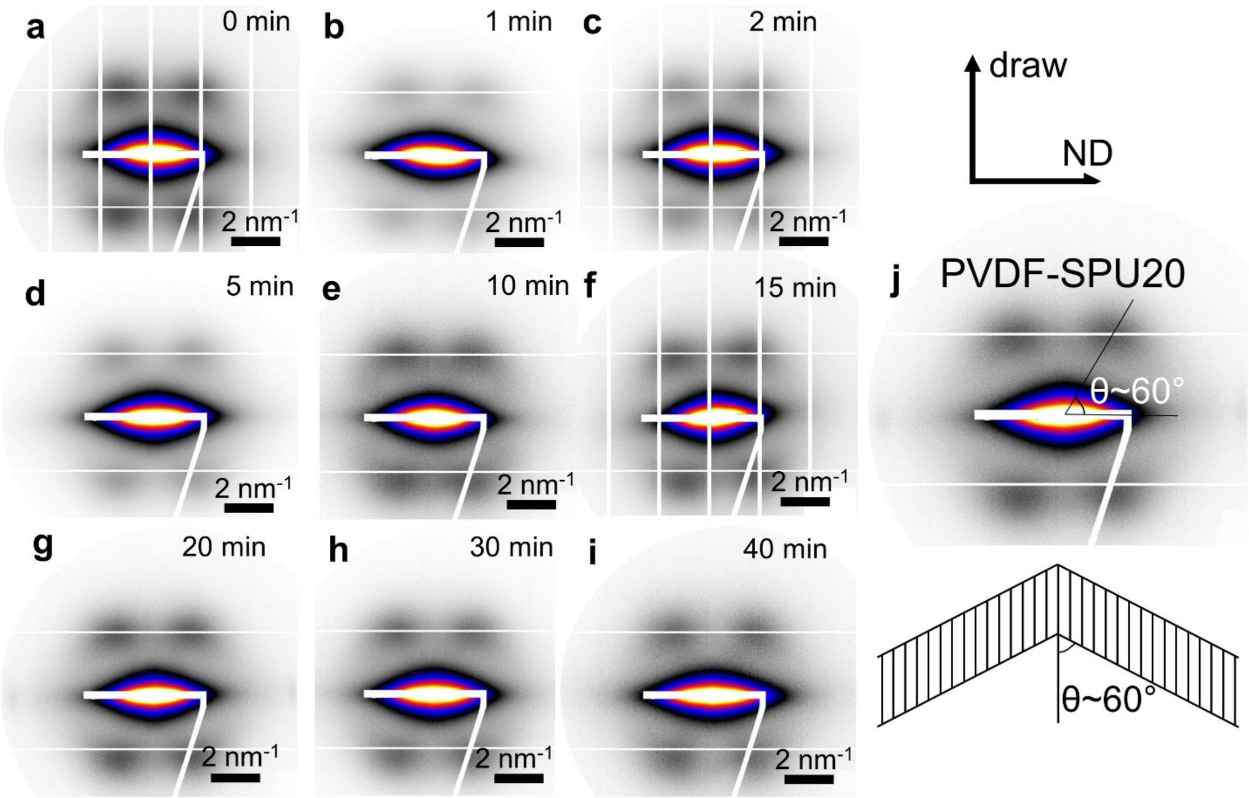

Fig. S3. 2D SAXS patterns for the uniaxially stretched PVDF-SPUx films at room temperature. The X-ray beam is directed along the transverse direction (TD) and the normal direction (ND) is in the horizontal direction. From the X-shaped patterns, the lamellar tilt angles from the drawing direction are found to be around 60° (the same for all samples).

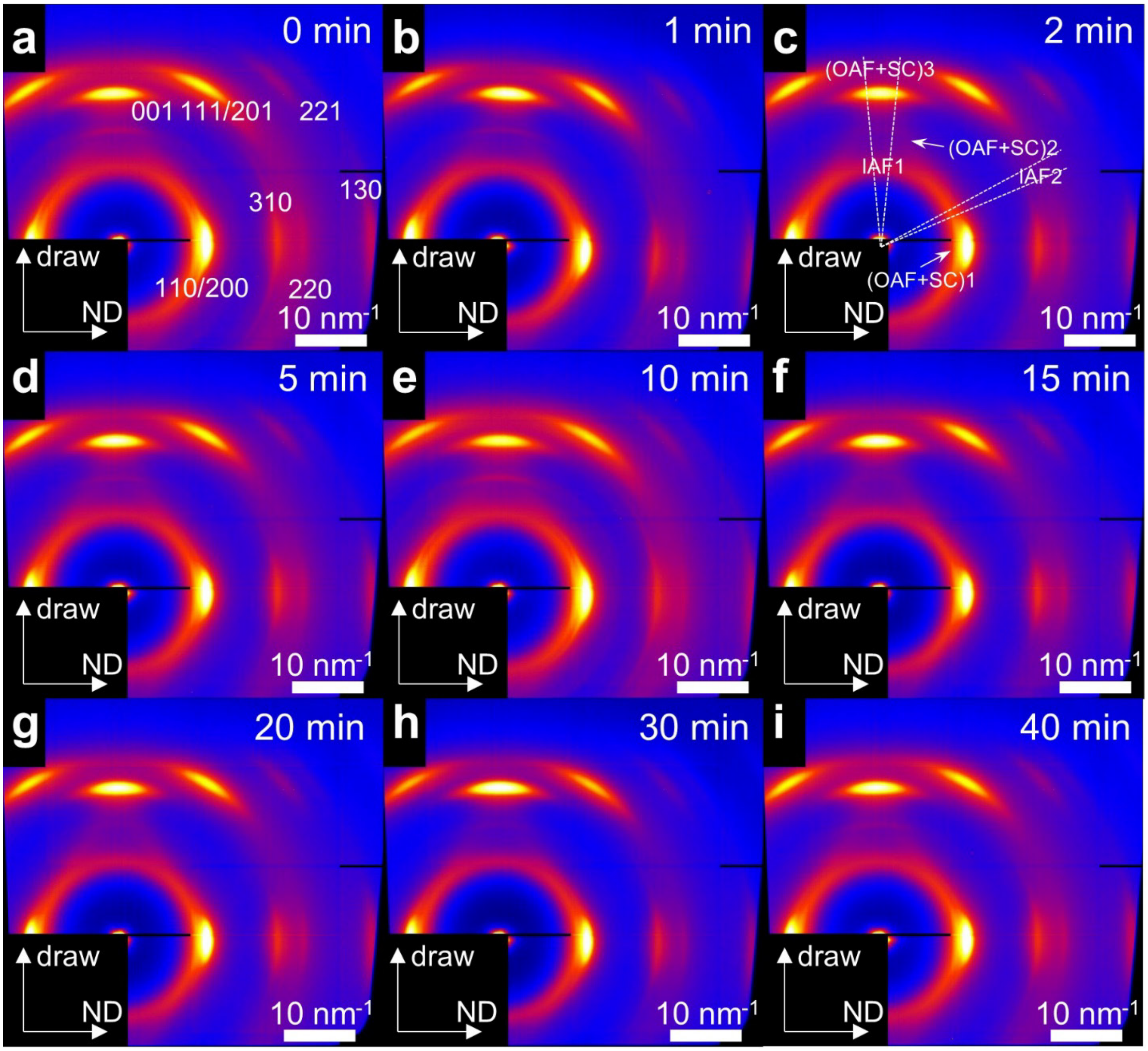

Fig. S4. 2D WAXD patterns of the uniaxially stretched PVDF-SPUx films at room temperature. The β phase reflections are labeled in (a). The X-ray beam is directed along the transverse direction (TD) and the normal direction (ND) is in the horizontal direction. (c) shows 2D WAXD analysis for IAF-inner (IAF1), IAF-outer (IAF2), (OAF+SC)1, (OAF+SC)2, and (OAF+SC)3. Details procedure should refer to our previous report.[3]

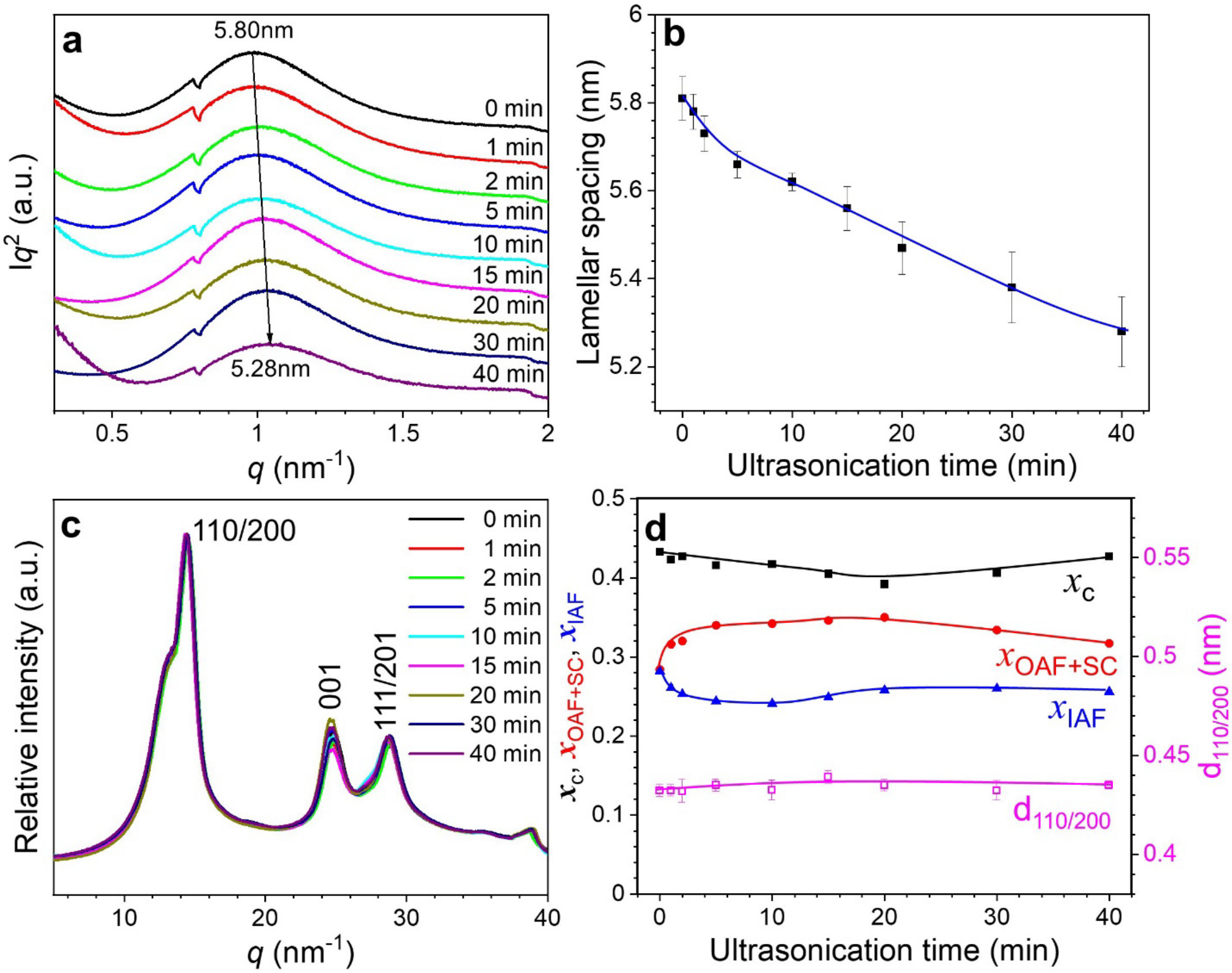

Fig. S5. a) Lorentz-corrected 1D SAXS profiles at room temperature and (b) the lamellar spacing quantified by the correlation analysis using SasView.[3] The correlation function analysis results are shown in Fig. S6. c) 1D WAXD curves for the PVDF-SPUx films at room temperature. d) x_c, x_{OAF+SC}, x_{IAF} from 2D WAXD analysis[3] and $d_{110/200}$ (= $2\pi/q_{110/200}$) as a function of the ultrasonication time. The detailed 1D WAXD peak-fitting results for all PVDF-SPUx samples are shown in Fig. S7.

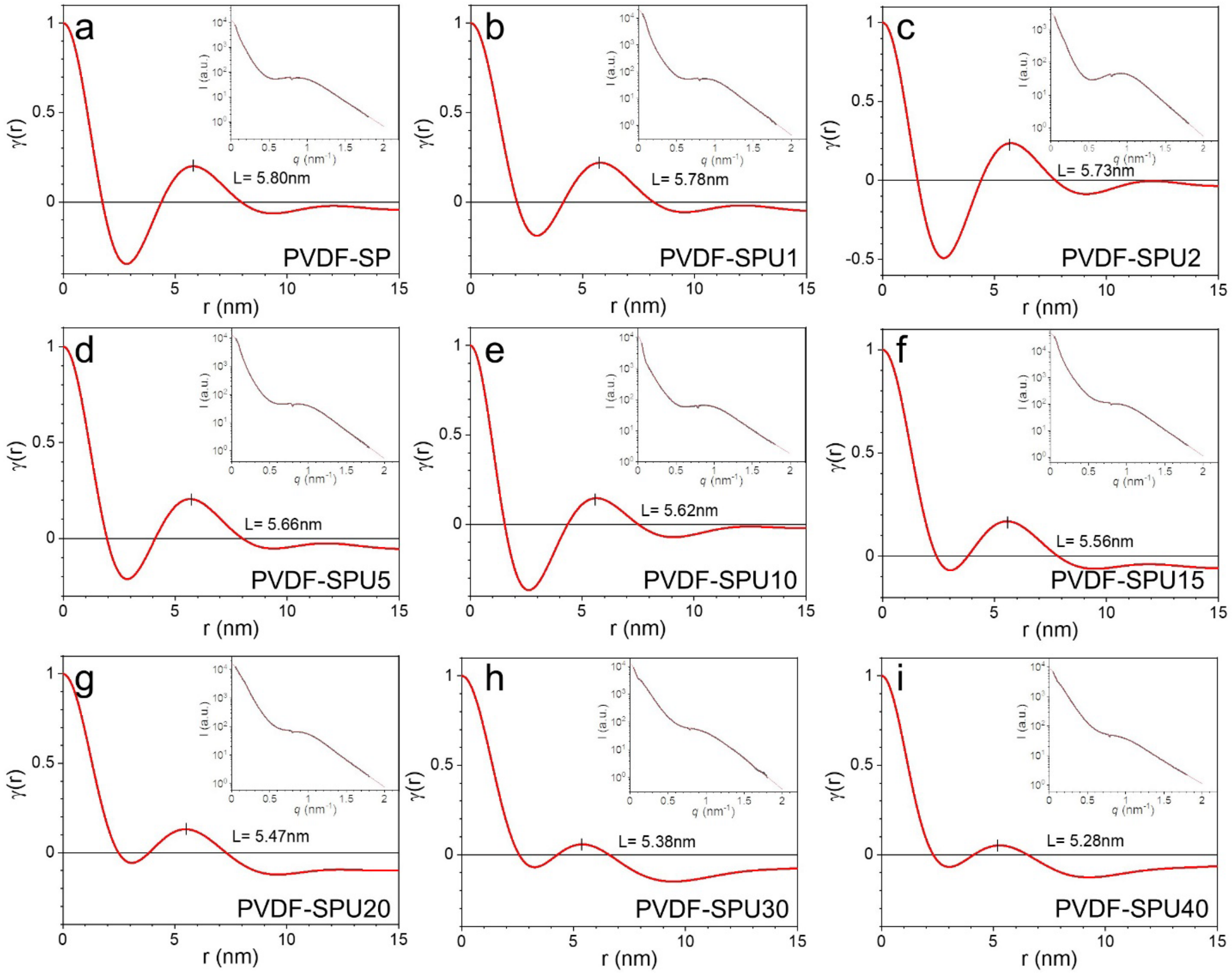

Fig. S6. Correlation function γ(r) of overall lamellar spacing for various PVDF-SPUx films using the SasView software.[3] The overall lamellar spacing (L) is taken as the distance (r) at the first maximum. The insets show the corresponding 1D SAXS profiles at room temperature.

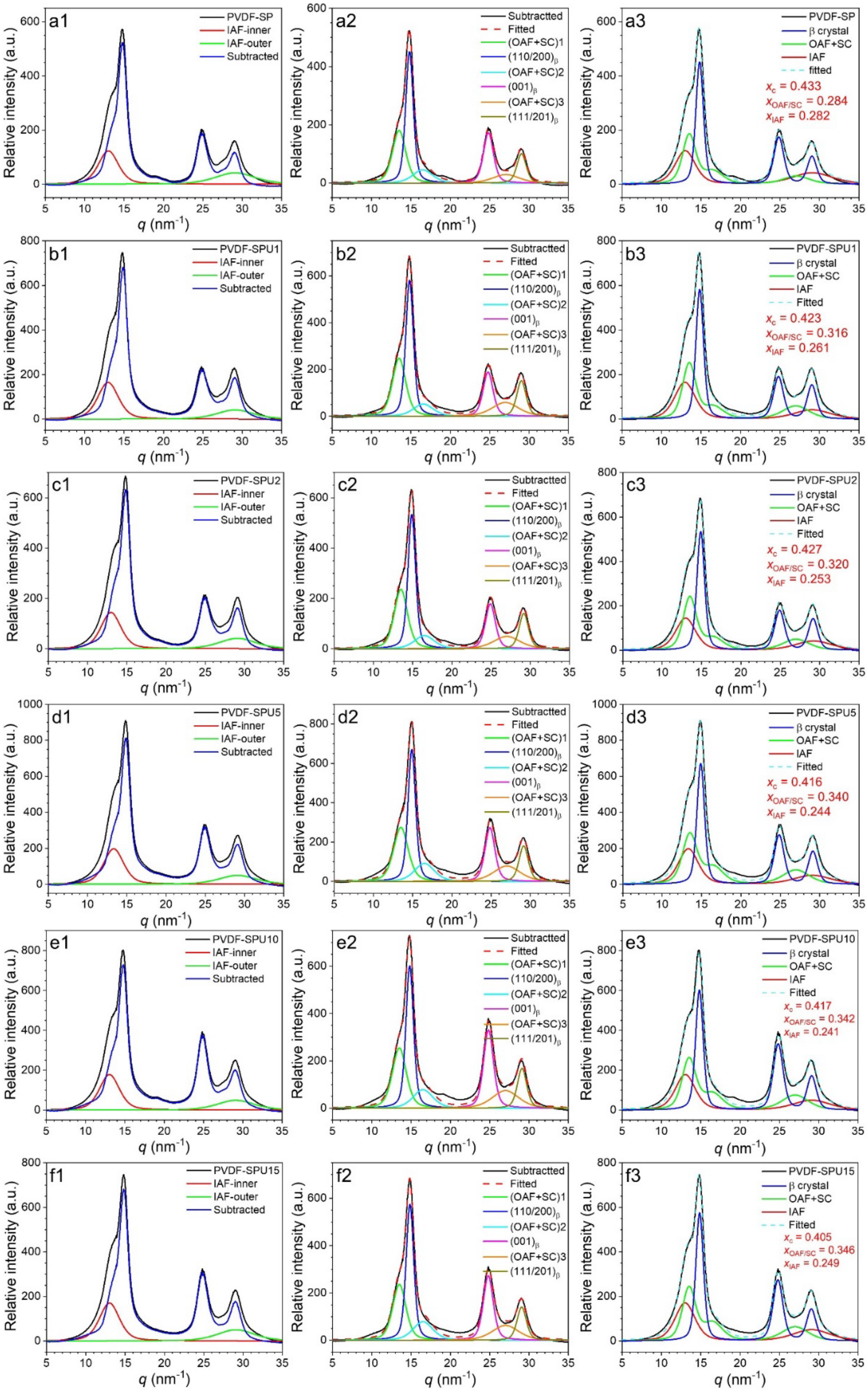

a1
PVDF-SP
IAF-inner
IAF-outer
Subtracted
a2
Subtractted
Fitted
(OAF+SC)1
$(110/200)_\beta$
(OAF+SC)2
$(001)_\beta$
(OAF+SC)3
$(111/201)_\beta$
a3
PVDF-SP
β crystal
OAF+SC
IAF
fitted
$x_c = 0.433$
$x_{OAF/SC} = 0.284$
$x_{IAF} = 0.282$
b1
PVDF-SPU1
b3
$x_c = 0.423$
$x_{OAF/SC} = 0.316$
$x_{IAF} = 0.261$
c1
PVDF-SPU2
c3
$x_c = 0.427$
$x_{OAF/SC} = 0.320$
$x_{IAF} = 0.253$
d1
PVDF-SPU5
d3
$x_c = 0.416$
$x_{OAF/SC} = 0.340$
$x_{IAF} = 0.244$
e1
PVDF-SPU10
e3
$x_c = 0.417$
$x_{OAF/SC} = 0.342$
$x_{IAF} = 0.241$
f1
PVDF-SPU15
f3
$x_c = 0.405$
$x_{OAF/SC} = 0.346$
$x_{IAF} = 0.249$
Relative intensity (a.u.)
q (nm^{-1})

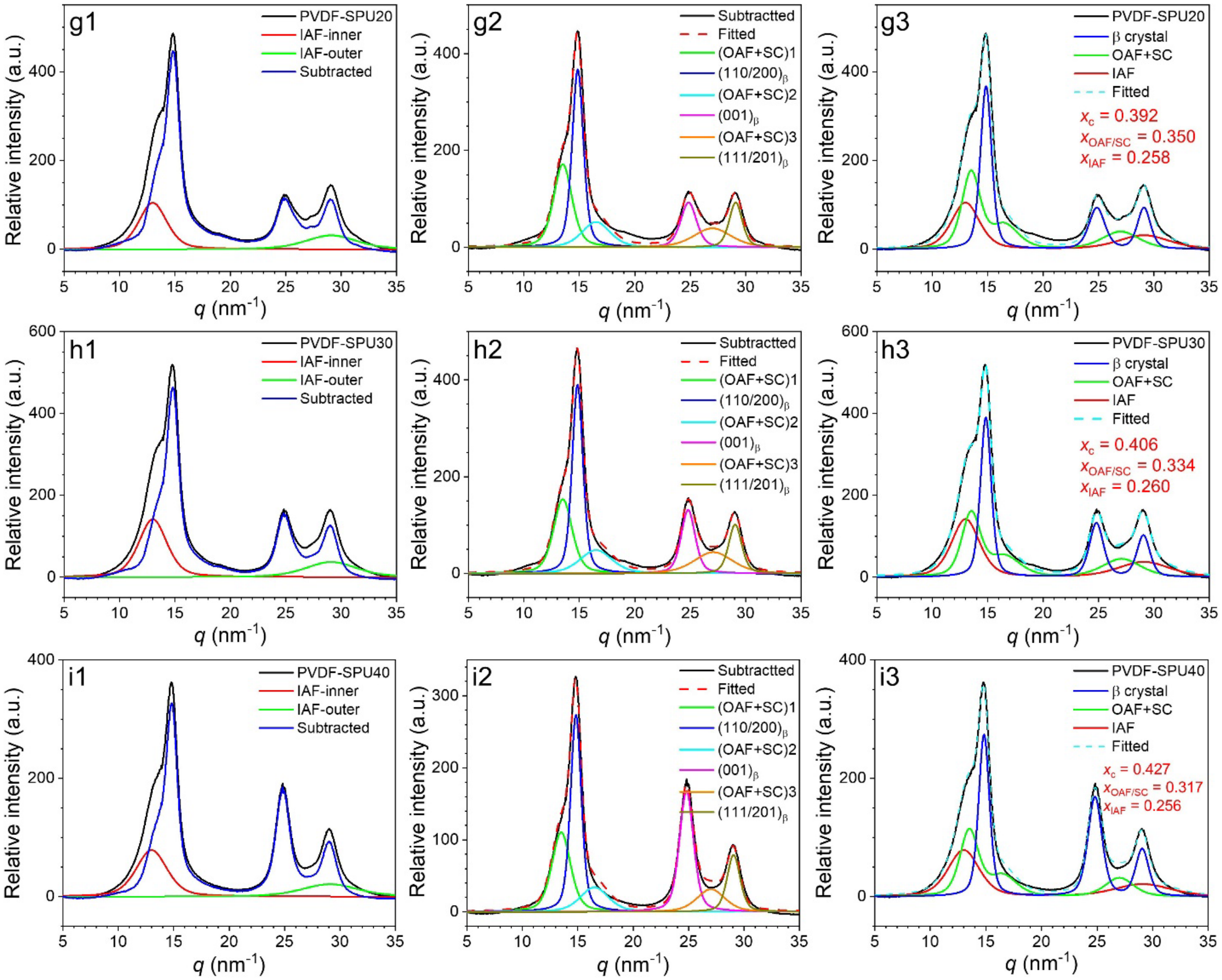

Fig. S7. WAXD analysis results for (a1-a3) PVDF-SP, (b1-b3) PVDF-SP1, (c1-c3) PVDF-SP2, (d1-d3) PVDF-SP5, (e1-e3) PVDF-SP10, (f1-f3) PVDF-SP15, (g1-g3) PVDF-SP20, (h1-h3) PVDF-SP30, and (i1-i3) PVDF-PS40. (1) Fitted IAF-inner, IAF-inner, and subtracted curve from the experimental WAXD profile. (2) Fitted (OAF+SC)1, $(110/200)_\beta$, (OAF+SC)2, $(001)_\beta$, (OAF+SC)3, and $(111/201)_\beta$ curves. (3) Overall fitted β crystal, OAF+SC, and IAF curves. The calculated x_c, x_{OAF+SC}, and x_{IAF} values are shown.

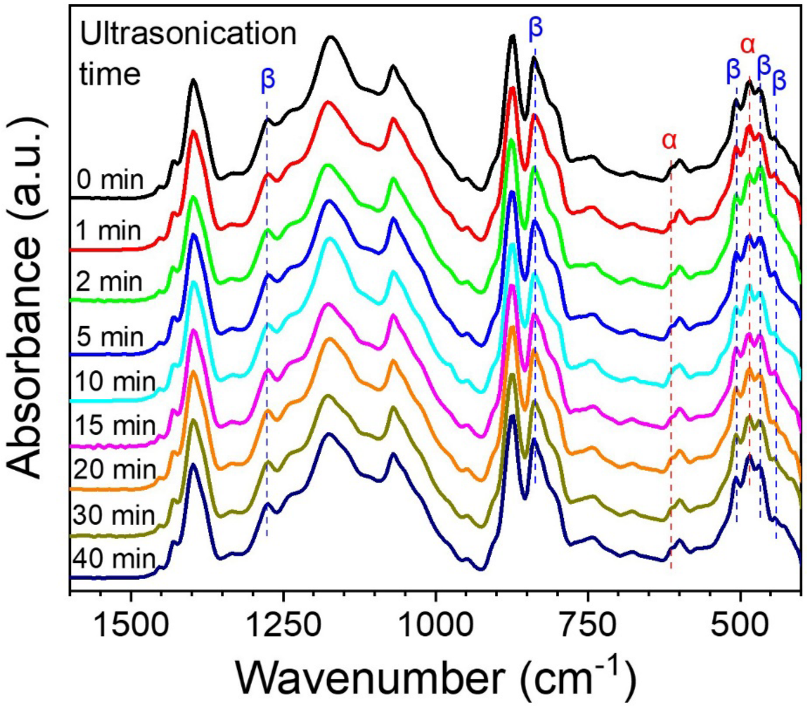

Fig. S8. Single-bounce diamond ATR FTIR spectra of various PVDF-SPUx films at room temperature.

4. DSC results for the PVDF-SPUx films

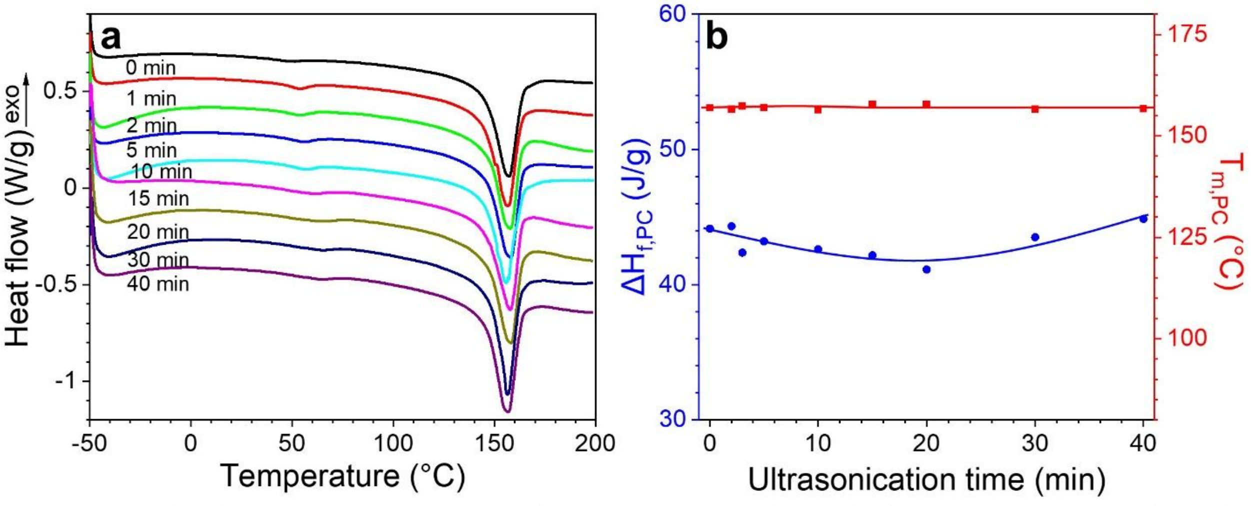

Fig. S9. a) First heating DSC curves for the PVDF-SPUx films. The heating rate is 10 °C/min. b) The primary crystal (PC) $\Delta H_{f,PC}$ and $T_{m,PC}$ as a function of the ultrasonication time.

5. Temperature-scan BDS results for the PVDF-SPUx films

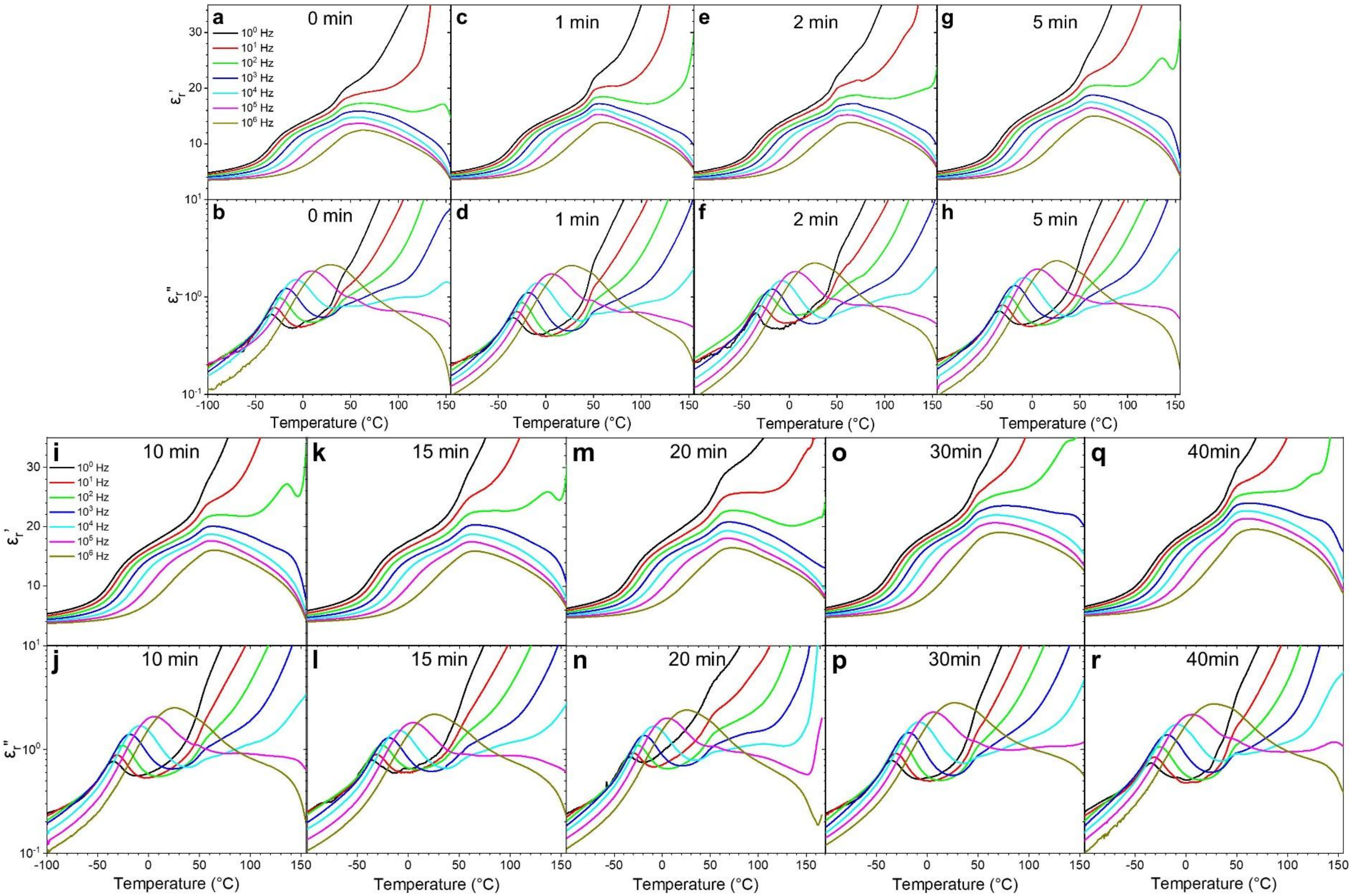

Fig. S10. Temperature-scan BDS results of (a,c,e,g,i,k,m,o,q) ε_r' and (b,d,f,h,j,l,n,p,r) ε_r'' for the PVDF-SPUx films. The heating rate was 2 °C/min. Above 100 °C, the stretched films started to shrink, causing decreased ε_r' for frequency ≥ 1 kHz.

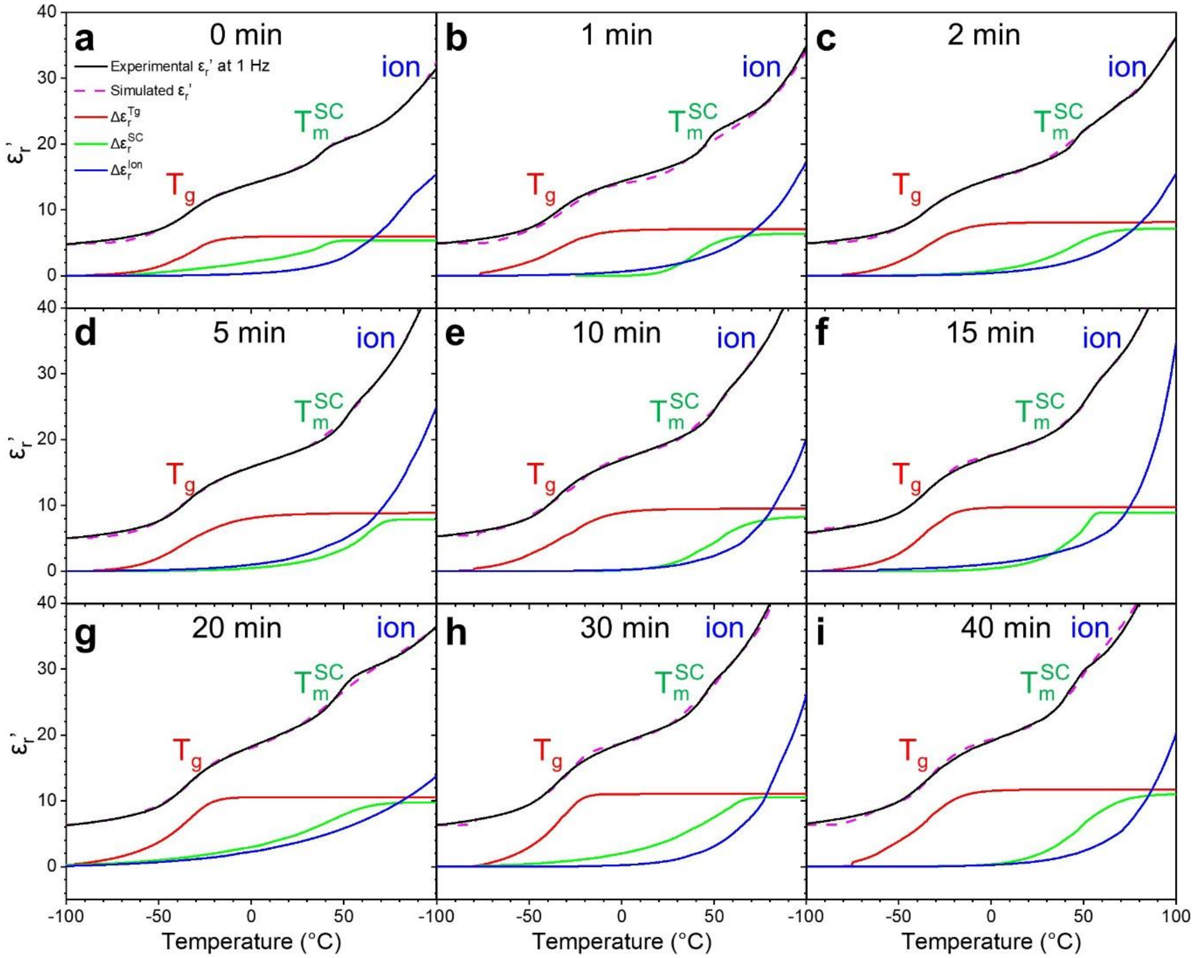

Fig. S11. Deconvolution results of the temperature-scan ε_r' curves of various PVDF-SPUx films at 1 Hz. The multimode Havriliak-Negami (HN) formula is used for the deconvolution, as reported before.[12,13] Three relaxation processes are simulated: glass transition (T_g), melting of SCs (T_m^{SC}), and ionic conduction, from which the ε_r' changes, $\Delta\varepsilon_r^{Tg}$, $\Delta\varepsilon_r^{SC}$, and $\Delta\varepsilon_r^{ion}$, are obtained.

6. Young's moduli for PVDF-SP and PVDF-SPUx films at different temperatures

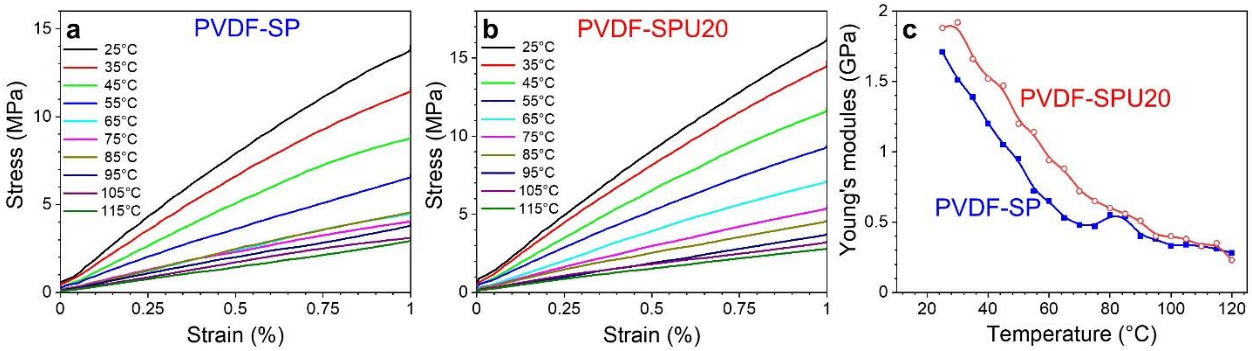

Fig. S12. Stress-strain curves of a) the PVDF-SP film and b) the PVDF-SPU20 film. c) Young's moduli of the PVDF-SP and the PVDF-SPU20 films as a function of temperature.

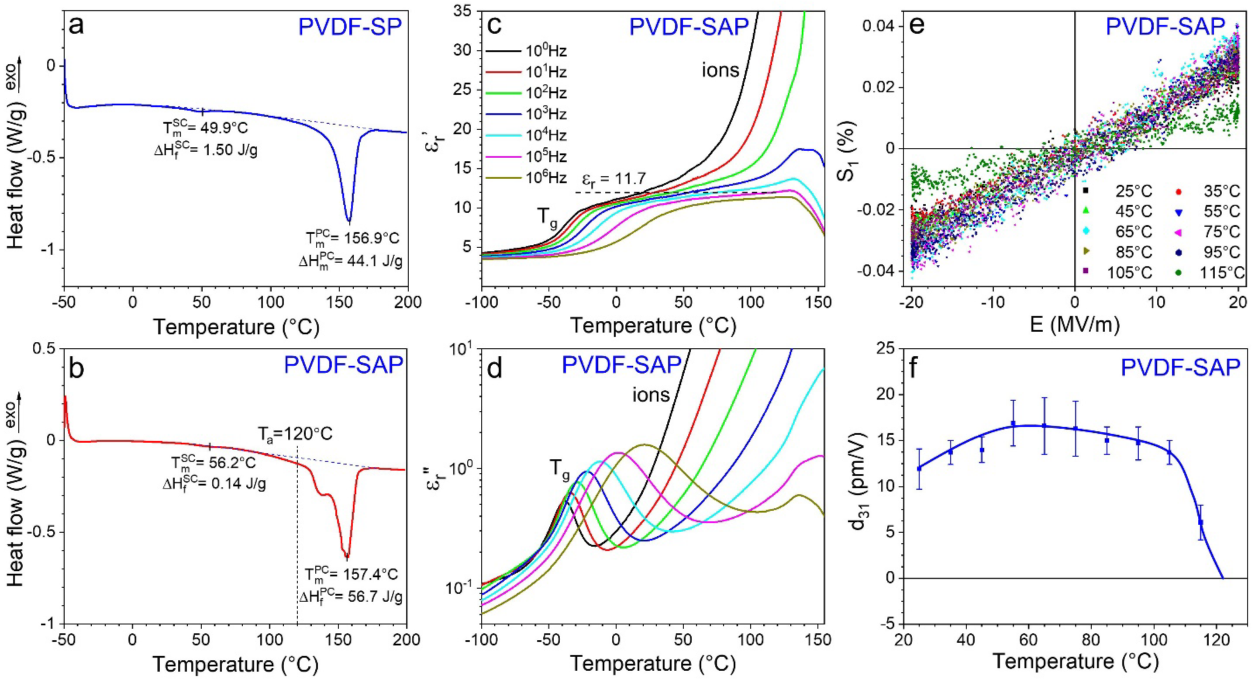

Fig. S13. First-heating DSC curves for (a) PVDF-SP and (b) PVDF-SAP films. The PVDF-SAP was obtained by annealing the PVDF-S film at 120 °C for 2 days, followed by unidirectional electric poling at 400 MV/m (10 Hz) and room temperature for 40 times. The heating rate is 10 °C/min. Temperature-scan BDS results of (c) ε_r' and (d) ε_r'' for the PVDF-SAP film under different frequencies. The heating rate is 2 °C/min. (e) Inverse piezoelectric S_1-E loops under bipolar poling at 20 MV/m (1 Hz) and (f) the d_{31} as a function of temperature for the PVDF-SAP film. Temperature is stepwise increased.

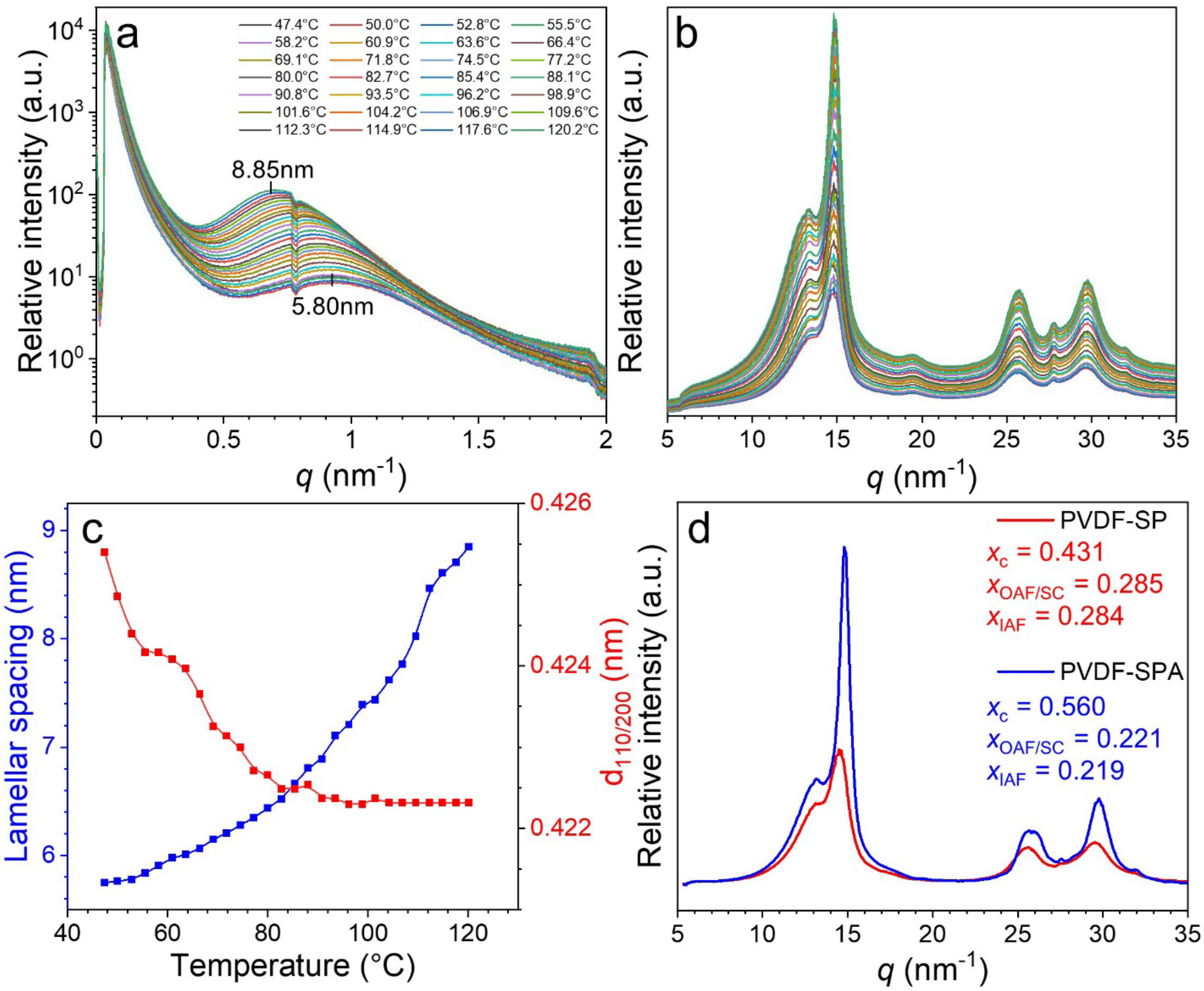

Fig. S14. 1D (a) SAXS and (b) WAXD profiles for the PVDF-SAP film at different temperatures. (c) Overall crystalline lamellar thickness (from SAXS) and $d_{110/200}$ (from WAXD) at different temperatures. (d) WAXD analysis results of x_c, $x_{OAF/SC}$, and x_{IAF} for the PVDF-SP and PVDF-SAP films.

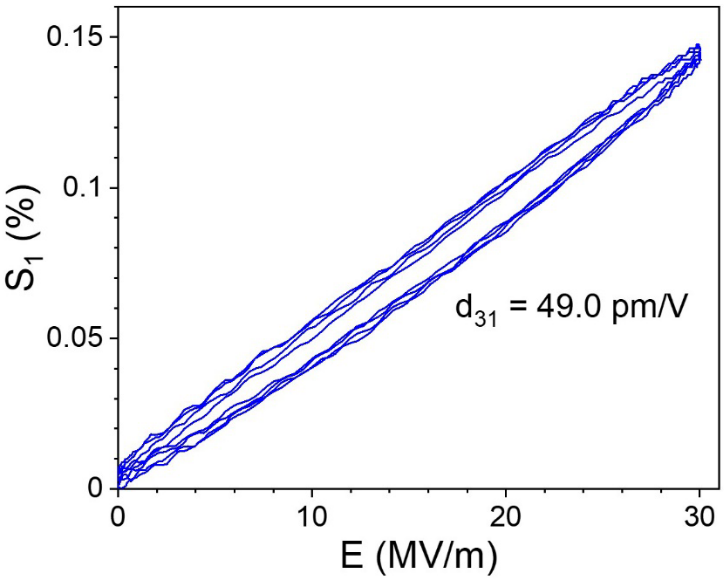

Fig. S15. Unipolar S_1-E loop for the hot-pressed PVDF film stretched with multiple steps up to 900% draw ratio at room temperature.

References

S1. Z. Cheng, V. Bharti, T. Xu, S. Wang, Q. M. Zhang, T. Ramotowski, F. Tito and R. Ting, *J. Appl. Phys.* 1999**, 86,** 2208-2214.

S2. T. Wongwirat, M. Wang, Y. Huang, I. Treufeld, R. Li, P. Laoratanakul*,* H. Manuspiya and L. Zhu, *Macromol. Mater. Eng.* 2019**, 304,** 1900330.

S3. Z. Zhu, G. Rui, Q. Li, E. Allahyarov, R. Li, T. Soulestin, F. Dos Santos, H. He, P. Taylor and L. Zhu, *Matter* 2021, **4,** 3696-3709.

S4. T. Furukawa and J. X. Wen, *Jpn. J. Appl. Phys.* 1984**, 23,** L677-L679.

S5. T. Furukawa, J. X. Wen, K. Suzuki, Y. Takashina, M. Date, *J. Appl. Phys.* 1984, **56,** 829-834.

S6. S. C. Mathur., J. I. Scheinbeim and B. A. Newman, *J. Appl. Phys.* 1984, **56,** 2419-2425

S7. Y. Huang, G. Rui, Q. Li, E. Allahyarov, R. Li, M. Fukuto, G. Zhong, J. Xu, Z. Li, P. L. Taylor and L. Zhu, *Nat. Commun.* 2021, **12,** 675.

S8. R. Zeng, K. W. Kwok, H. L. W. Chan and C. L. Choy, *J. Appl. Phys.* 2002, **92,** 2674.

S9. M. Nagai, K. Nakamura, H. Uehara, T. Kanamoto, Y. Takahashi and T. Furukawa, *J. Polym. Sci., Part B: Polym. Phys.* 1999, **37,** 2549-2556.

S10. W. Yan, G. Noel, G. Loke, E. Meiklejohn, T. Khudiyev, J. Marion, G. Rui, J. Lin, J. Cherston, A. Sahasrabudhe, J. Wilbert, I. Wicaksono, R. W. Hoyt, A. Missakian, L. Zhu, C. Ma, J. Joannopoulos and Y. Fink, *Nature*, 2022, **603**, 616-623.

S11. J. Gao, D. Xue, W. Liu, C. Zhou and X. Ren, *Actuators* 2017, **6,** 24.

S12. X. Chen, E. Allahyarov, Q. Li, D. Langhe, M. Ponting, D. Schuele, E. Baer and L. Zhu, *Compos. B: Eng.* 2020, **190,** 107908.

S13. X. Chen, E. Allahyarov, D. Langhe, M. Ponting, R. Li, M. Fukuto, D. Schuele, E. Baer and L. Zhu, *J. Mater. Chem. C* 2020, **8,** 6102-6117.